Dual-Carrier-Paired Point-to-Multipoint Transmission Over ROADM Systems: Frequency-Polarization Coding and Frequency Collaborative Control

Takahiro Kodama, *Member, IEEE*, and Ryosuke Matsumoto, *Member, IEEE*

***Abstract*—In dual-carrier (DC)-paired fiber optic long-reach transmission, which extends a point-to-multipoint coherent system to a cascaded reconfigurable optical add-drop multiplexing (ROADM) system, a narrow passband causes severe performance degradation of the edge subcarriers. In this study, we proposed two-dimensional frequency and polarization domain coding and multicarrier-frequency control for cascaded ROADM filtering of robust multicarrier transmissions at a single wavelength. The proposed coding scheme reduced fiber nonlinearity, polarization-dependent loss (PDL), and passband narrowing (PBN) simultaneously. The multicarrier frequency control algorithm, which feeds back the received signal quality at multiple points, reduced PBN owing to long-term laser frequency drifts. With the proposed coding, the Q value of 56 Gbit/s × DC-paired dual-polarized (DP)-4QAM and 112 Gbit/s × DC-paired DP-16QAM signals improved by 1 dB and 0.2 dB, respectively, compared to that when no coding was used. Furthermore, the long-term frequency control emulated through the emulation model of laser frequency drifts and the performance degradation of average Q value were less than 0.4 dB and 0.1 dB, respectively. To the best of our knowledge, no other study has evaluated point-to-multipoint transmission over ROADM-induced optical filtering systems that apply frequency and polarization domain coding and multicarrier frequency control for DC-paired DP-*M*-QAM signals. The proposed methods enable stable operation while suppressing the effects of PDL and PBN, which are problems in multicarrier transmission, in long-reach optical fiber transmission systems that integrate access and metro networks.**

***Index Terms*—Optical communication, quadrature amplitude modulation, frequency division multiplexing, fiber nonlinearity, polarization-dependent loss, passband narrowing.**

I. Introduction

MANY networks that target aggregation with metro networks are hub-and-spoke in nature, with many spoke devices (e.g., fiber node, cell site optical line terminal) connected to a few hub devices (e.g., router, evolved packet core/next-generation core, broadband network gateway). However, the optical technology that underpins these networks is always point-to-point, with individual optical transceivers having the same speed at each end. This mismatch causes high capital and operation expenditures owing to the large number of inefficiently used optical transceivers and router ports, and multiple layers of packet aggregation [1]. Additionally, it is expected to become more severe with the evolution of access networks, which includes mobile to 5G, cable to distributed access architecture, and passive optical networks to next-generation passive optical network (PON) technology. As a result, both the bandwidth and the number of spoke devices would increase significantly. After combining the subcarriers as multi-subcarrier wavelengths, this multicarrier signal can be transferred via a flexible grid reconfigurable optical add-drop multiplexing (ROADM) network or a fixed grid wavelength division multiplexing (WDM) infrastructure tuned into the required spectrum, as shown in Fig. 1. The transmission distances of the 1,000 km-class and 4,000 km-class 16 quadrature amplitude modulation (QAM) multicarrier system and 4QAM multicarrier system, respectively, enable cost-effective centralization of hub resources [2]. Fig. 1 shows a colorless, directionless, contentionless, and gridless (CDCG)-ROADM node configuration. Each ROADM node comprises a wavelength-selective switch (WSS) and a multicast switch, which generally comprises an optical switch and an optical coupler [3].

In optical metro network systems over current ROADM nodes, linear distortions such as chromatic dispersion (CD) can be entirely compensated using commercialized digital signal processing (DSP). However, nonlinear optical effects limit the capacity of the fiber link [4]–[6]. Furthermore, as the baud rate in the DSP shifts from a 28 GBd class to a 56 GBd class, the fiber nonlinear effects increases [7]. A cost-effective approach to reuse optical and electrical components for low baud rates is dual-carrier (DC) modulation, which requires two optical carrier modulation signals [8], [9]. Conversely, high baud rate transceivers with flexible modulation formats using advanced DSP techniques, which accommodate various data-traffic demands and fiber-link conditions by spectral efficiency (SE) modifications, are considered suitable for elastic optical

Manuscript received March 22, 2022; revised May 1, 2022; accepted May 12, 2022. Date of publication May 25, 2022; date of current version May 30, 2022. This work was supported by JSPS KAKENHI under Grant JP22K04105. *(Correspondig author: Takahiro Kodama.)*

Takahiro Kodama is with the Faculty of Engineering and Design, Kagawa University, Takamatsu, Kagawa 761-0396, Japan (e-mail: kodama.takahiro@kagawa-u.ac.jp).

Ryosuke Matsumoto is with the National Institute of Advanced Industrial Science and Technology, Tsukuba, Ibaraki 305-8568, Japan (e-mail: matsumoto.ryosuke@aist.go.jp).

Digital Object Identifier 10.1109/JPHOT.2022.3175365

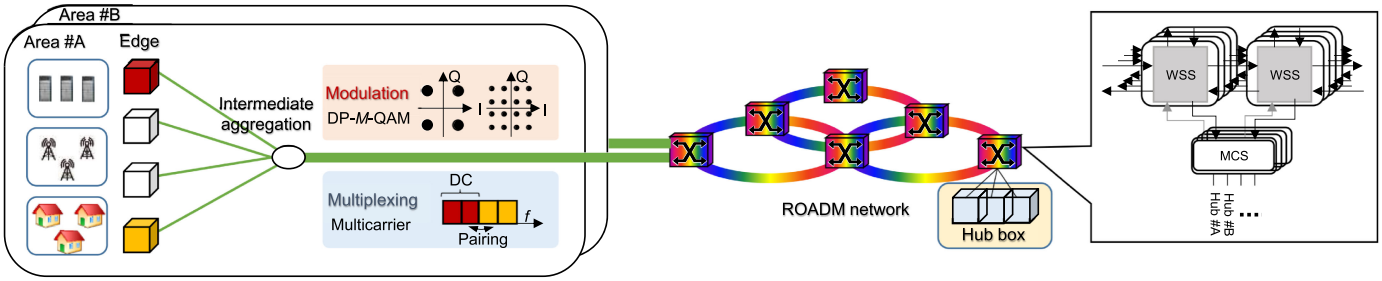

Fig. 1. Physical topology of access and metro aggregated network over CDCG-ROADM.

networks. While the transmission distance can be increased by compensating for the fiber nonlinear effects through DSP on the receiving side, a considerable circuit scale is required to obtain sufficient compensation effect [10], [11]. Frequency-division subcarrier (SC) multiplexing in the digital domain is a promising technique as it reduces the fiber nonlinearity and complexity of the receiver-side DSP for CD compensation [12], [13]. Each SC is shaped using root-raised-cosine (RRC) filtering in the transmitter-side DSP, and is arranged at frequency spacings close to the Nyquist limit [14]. Recently, a cost-effective multicarrier-coherent receiver [15]–[18] with a single local oscillator capable of receiving Nyquist-shaped SC multiplexing signals simultaneously. However, the performance of SC multiplexed signals further decreases owing to polarization-dependent losses (PDLs) in optical transceivers or ROADM nodes [19], [20] and cascaded WSSs in ROADM-node-induced passband narrowing (PBN) [21]. In ring or meshed OTN systems comprising several cascaded ROADM nodes for different path links, the pass-band bandwidth of WSSs varies owing to the effects of the PBN caused by ROADM nodes [22], [23]. As the number of modulation degrees increases, the signal characteristics due to the PBN decreases.

Inter-subcarrier and inter-polarization coding schemes have been proposed for multi-carriers to reduce the performance degradation of edge SCs [24]–[27]. Furthermore, methods such as spectral power monitoring and control [28], [29], PDL monitoring [30], spectral manipulation [31]–[33], spectral-domain hybrid modulation [34], and path-fitted pre-filtering schemes [35] have been proposed to increase the tolerance of fiber nonlinearities with strict filtering. Recently, edge- and middle-SC signals with variable probabilistic-shaped constellations have been proposed to improve PBN tolerance [36]. Recently, frequency and polarization concatenated coding (FPCC), a simple combination of frequency and polarization-domain phase-conjugate coding in DSP, has been proposed to simultaneously mitigate fiber nonlinearity, PDLs, and PBN [37], [38]. However, if either approach is used by setting the optimum frequency allocation at the beginning of life, the edge subcarriers can cause significant performance degradation owing to the long-term frequency drifts of laser diodes (LDs) or WSSs at ROADM nodes [39]. Therefore, multicarrier frequency control algorithms for single-wavelength light sources [40] are simpler compared to multicarrier frequency control algorithms for multiwavelength sources used in superchannel signals [35]. However, no study has evaluated point-to-multipoint transmission over ROADM-induced optical filtering systems that apply frequency and polarization domain coding and multicarrier frequency control for DC-paired DP-*M*-QAM signals.

The FPCC and multicarrier frequency control algorithms have been applied to the dual-polarization *M*-ary QAM (DP-*M*-QAM) for the situations where constant optimization of the signal point level is complicated in ROADM systems where the center frequencies of the light source and WSS are unstable. This study is an extension of the work reported in [37], [38]. The novelty of this study is that the frequency control in multicarrier transmission is expanded from point-to-point to point-to-multipoint topology. To ignore the fiber nonlinear effects, we also evaluated the back-to-back characteristics of the proposed multicarrier coding for DC-paired multicarrier signals.

The remainder of this paper is organized as follows. Section II introduces a system configuration of coherent Nyquist-WDM (N-WDM) over a ROADM system with a point-to-multipoint topology. Section III presents the principles of FPCC. Section IV describes the operation of the multicarrier frequency-control algorithm. Section V describes the system setup. Section VI presents the numerical simulations of a 56 GBd DP-*M*-QAM signal ($M = 4$ and 16) using FPCC, wherein static performance under both single carrier and DC-paired multicarrier signals for the same spectral efficiency of 4 and 8 bit/s/Hz have been demonstrated. We observed the performance of the 4SC-DP-4QAM and 4SC-DP-16QAM signals with FPCC. Section VII evaluates the dynamic characteristics of the 56 GBd DP-*M*-QAM signals ($M = 4$ and 16) using FPCC and a multicarrier frequency control algorithm, assuming LD frequency drifts for an extended time period. By using the proposed frequency control algorithm with a collaborating transmitter and receiver via dynamic characteristics by the emulator program, an improvement in Q was observed in the presence of linear LD frequency drifts with only $+/-2.5$ GHz.

II. Nyquist-Shaped WDM-Based DC-Paired Transmission Over a ROADM System With Point-to-Multipoint Topology

Fig. 2 shows the architecture of the full-duplex uplink/downlink with two SMFs and the operation of a coherent N-WDM system with a point-to-multipoint topology. The

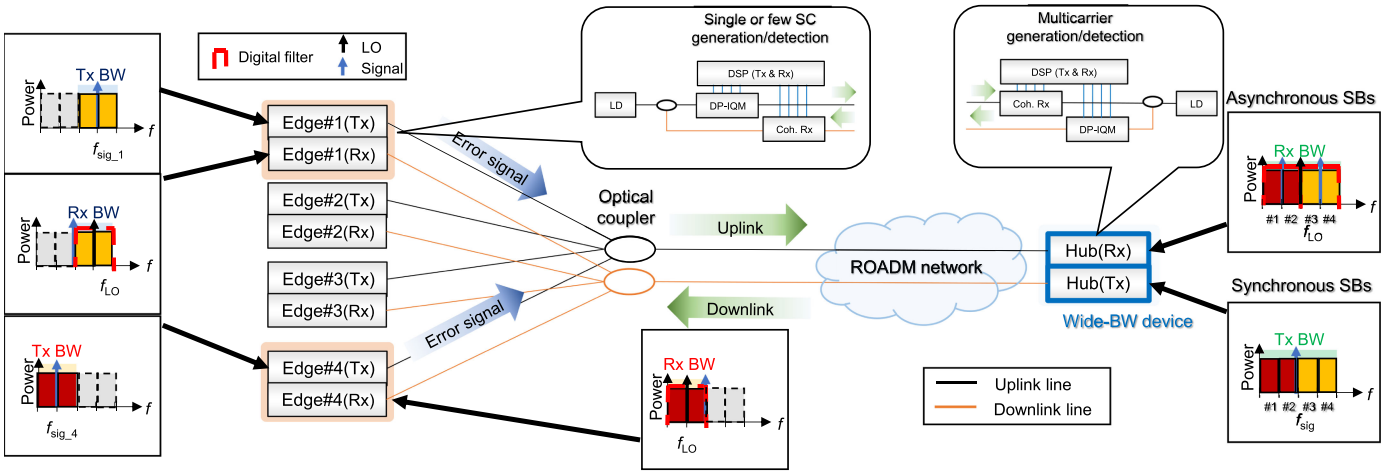

Fig. 2. System configuration of coherent N-WDM-based DC-paired transmission over ROADM system with point-to-multipoint topology.

feature of the full-duplex transmission configuration is that even if one light source is shared with the transmitter and receiver, no effect of backward Rayleigh scattering and Fresnel reflection occurs.

The bandwidths of the radio frequency (RF) and optical analog devices are asymmetric between the edge and hub sites, which reduces the total transceiver cost of point-to-multipoint topologies. Wideband RF devices, such as analog-to-digital converters (ADCs) and digital-to-analog converters (DACs), are placed in the hub, and the narrowband RF and optical analog devices are placed at the edges. Each SC signal uses adaptive modulation and a baud rate, which allows the modulation method to be selected while meeting the required transmission rate. For example, for the same low baud rate and low-level modulation format type of 14 GBd/SC DP-4QAM for all SC signals, the edge data rate was set to 56 Gb/s/SC-class signal. In contrast, for the same high baud rate and high-level modulation format type 14 GBd/SC DP-16QAM for all SC signals, the edge data rate was set to 112 Gb/s/SC-class signal.

In the uplink, the transmission rate of each edge transceiver varied depending on the application. For large-traffic applications from edge transceivers, the transmission rate used per edge transceiver is 100 Gb/s-class. If there is a small traffic application from the edge transceiver, the transmission rate used for each edge transceiver is 50 Gb/s-class. The primary uplink method is multicarrier coherent detection, which comprises a single coherent receiver that employs a wideband ADC, digital domain spectrum filter, and a heterodyne detection method. At the edge transmitter, *a K* SC signal is generated and sent to the access span. Each SC signal is coupled using an optical coupler that corresponds to a remote node and is transmitted over the trunk span. The receiver at the hub site uses a local oscillator to collectively detect asynchronous multiplexed SC signals depending on the number of edges accessed. Therefore, multiple application traffic signals were effectively processed by a single DSP chip.

SC was assigned to each edge adaptively depending on the number of edge accesses, similar to the uplink on the downlink. The primary downlink technique is SC assembly generation comprising a single in-phase quadrature modulator (IQM) with a wideband DAC and a digital domain spectral filter. The hub transceiver sends the K-SC to the trunk span per SC signal generated by the transmitter. The SC multiplexing signal was split by an optical coupler and sent to each access span. The edge on the receiver side uses a local oscillator to select the desired band depending on the downlink rate of the edge for colorless operation. To demonstrate the flexible rate-coherent N-WDM transceiver for the ROADM system with point-to-multipoint topology, we developed a multicarrier transceiver that performs data rate and modulation adaptive methods to meet the asymmetric traffic demand. Optical switches and transponders, which are physical layer technologies, envisioned a new 12.5 GHz flex grid that supports ultrafine particles much lower than traditional ITU-T 50 GHz fixed grids. The multicarrier concatenated coding introduced in Section III can be used for both uplink and downlink transmissions. Therefore, considering the performance characteristics of the uplink and downlink transmissions are the same, only the downlink simulation is performed. The collaborative frequency control introduced in Section IV can be applied to downlink transmissions considering the signals at multiple points are fed back and controlled collectively. The feedback error signal is propagated from the edge to the hub by a management signal such as an auxiliary management and control channel (AMCC) [41].

III. Two-Dimensional Frequency/Polarization-Concatenated Coding Scheme

Herein, we describe three types of coding principles. If the PDL and PBN cause a power difference between polarizations or frequencies owing to the transmission line, polarization coding (PC) and frequency coding (FC) are applied. If both are large, FPCC is selected. Fig. 3 shows a conceptual diagram based on the spectra of the four DC paired DP-*M*-QAM systems. Table I summarizes the expressions used for encoding and decoding in the three coding schemes. Two or four parallelized original signals E_i, where i is the data index ($i \in \{A, B, C, D\}$) are converted

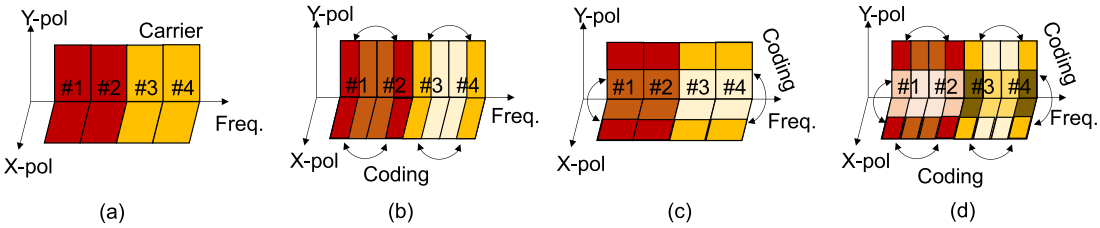

Fig. 3. Optical spectrum of DC-paired DP-M-QAM. (a) Standard, (b) FC, (c) PC, and (d) FPCC.

TABLE I
EQUATIONS OF ENCODING AND DECODING

Code type	Encoding	Decoding
FC	$E_E^{'} = E_A + E_B$ $E_M^{'} = E_A^* - E_B^*$	$E_A = E_E^{'} + E_M^{'*}$ $E_B = E_E^{'} - E_M^{'*}$
PC	$E_X^{'} = E_A + E_B$ $E_Y^{'} = E_A^* - E_B^*$	$E_A = E_X^{'} + E_Y^{'*}$ $E_B = E_X^{'} - E_Y^{'*}$
FPCC	$E_{EX} = E_A + E_B + E_C + E_D$ $E_{EY} = E_A^* + E_B^* - E_C^* - E_D^*$ $E_{MX} = E_A^* - E_B^* + E_C^* - E_D^*$ $E_{MY} = E_A - E_B - E_C + E_D$	$E_A = E_{EX} + E_{MX}^* + E_{EY}^* + E_{MY}$ $E_C = E_{EX} + E_{MX}^* - E_{EY}^* - E_{MY}$ $E_B = E_{EX} - E_{MX}^* + E_{EY}^* - E_{MY}$ $E_D = E_{EX} - E_{MX}^* - E_{EY}^* + E_{MY}$

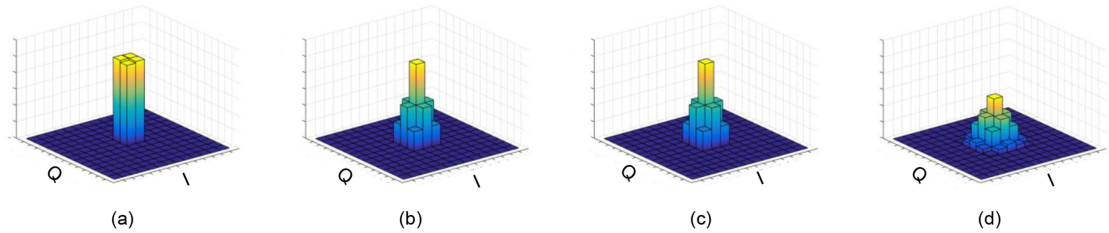

Fig. 4. Constellation. (a) Standard DP-4QAM, (b) FC, (c) PC, and (d) FPCC.

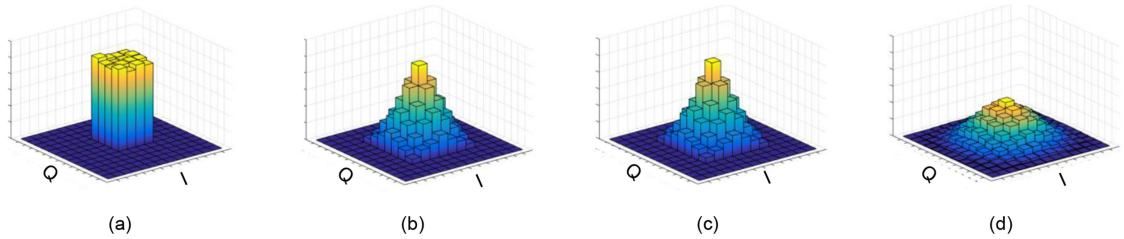

Fig. 5. Constellation. (a) Standard DP-16QAM, (b) FC, (c) PC, and (d) FPCC.

to the encoded signal E_{jk}, where j is the SC index ($j \in \{E, M\}$) and k is the polarization index ($k \in \{X, Y\}$). Figs. 4 and 5 show the histograms of the constellation maps of each SC for DP-4QAM and DP-16QAM, respectively. Under the four conditions shown in Fig. 3(a)–(d), the same distributed constellation was obtained for all four SCs. The DC-paired DP-M-QAM signals with FC and PC exhibited a pseudo-Gaussian distributed constellation of M' ($= 4M - 4\log_2 M + 1$)points with different probabilities of occurrence. Furthermore, there is a feature that the probability of occurrence increases toward the center of the signal point. These signals share data between frequencies or polarizations. The DC-paired DP-M-QAM signals using the FPCC signal also appear as a Gaussian probability distribution comprising M'' ($= 4M' - 4\log 2M' + 1$)-points, such as the one-dimensional coding FC and PC. For the FPCC signal, the probability of signal point 0 is lower than that for the standard DP-M-QAM, FC, and PC. The four original datasets were shared by both frequency and polarization domains. All decoded SC signals were recovered to the standard DP-M-QAM constellations.

IV. MULTICARRIER FREQUENCY CONTROL ALGORITHM

There are integrable tunable laser assembly (ITLA) and further miniaturized μ-ITLA as tunable light sources standardized

TABLE II
COMPARISON BETWEEN PROPOSED AND OTHER METHODS OF MULTICARRIER FREQUENCY CONTROL

	Error signal	Deterioration factor	Control interval	Deterioration due to dither signal
Ref. [30]	Spectrum power	PBN	Regularly	No
This work	Q factor	PBN, SC interference	Ordinarily	Yes

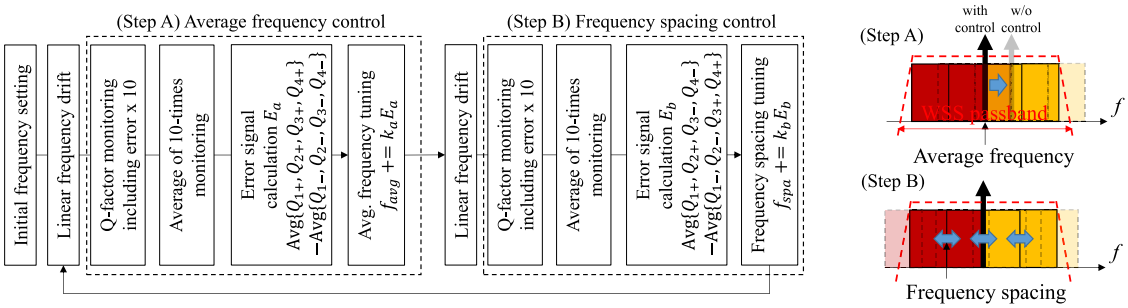

Fig. 6. Flowchart of subcarrier frequency control.

by Optical Internetworking Forum (OIF), and the maximum center frequency error of ITLA and μ-ITLA is +/− 2.5GHz and +/− 1.5GHz, respectively. Table II summarizes the technical differences between the method in ref. [30] and the proposed method for multi-carrier frequency control for ROADM systems. Here, we assume ITLA with a large frequency error is used. The proposed control has the same mechanism as a proportional, integral, and differential control implemented in two stages. The target value in each step is the center light frequency and the frequency interval of the subcarriers when the Q value is maximized. There are 2^K combinations of bipolar dithers for each SC. Therefore, as the number of SCs increases, the number of combinations increases exponentially, complicating the control procedure. Consequently, the process for controlling the optical frequencies of multiple SCs needs to be simplified. Fig. 6 shows the flowchart of the proposed frequency control algorithm for point-to-multipoint transmission via the ROADM network, which comprises two steps (steps A and B). This frequency-control algorithm can also be applied to regular ROADM networks. In the first step, the average frequency is optimized to maximize the average Q of all SCs. If it deviates from the optimum center frequency, the characteristics of either of the subcarriers will deteriorate significantly. In the second step, the frequency spacing is optimized for the average Q of all SCs. If the frequency interval deviates from the optimum frequency interval, the characteristics of either the inner or edge SCs are deteriorate significantly. We label the average Q of the SCs as Q_i and Q_{i_j}, where $i$is the SC number ($i \in \{1,2,\lessdot, K\}$), and j is the polarity of the frequency dithering ($j \in \{+, -\}$). Here, the average Q is defined as Avg$\{Q_{i_j}\}$ for the frequency dithering case. At each Step $S \in \{A, B\}$, by multiplying the calculated error signal E_s by coefficient $k_s (s \in \{a, b\})$, the average frequency f_{avg} and frequency spacing f_{spa} are updated relatively, such that E_s approaches zero without being treated as an absolute frequency. The error signals E_a and E_b are expressed as follows.

$$E_a = \text{Avg}\{Q_{1+}, Q_{2+}, Q_{3+}, Q_{4+}\} - \text{Avg}\{Q_{1-}, Q_{2-}, Q_{3-}, Q_{4-}\} \quad (1)$$

$$E_b = \text{Avg}\{Q_{1+}, Q_{2+}, Q_{3-}, Q_{4-}\} - \text{Avg}\{Q_{1-}, Q_{2-}, Q_{3+}, Q_{4+}\} \quad (2)$$

The error signal E_s is fed back to the optical transmitter via the transmission line. Then, the optical frequency drift caused by the light source of each SC is compensated by fine-tuning the central optical frequency of the light source. Frequency dithering and spacing for the average frequency control of Steps A and B, respectively, used as the fine control function of LDs and the frequency-shift function of transmitter-side DSP, respectively.

V. SIMULATION SETUP AND RESULTS

Fig. 7 shows a block diagram of a DC-paired multicarrier transmission system comprising a block of encoder/decoder and multicarrier frequency control. Considering this evaluation excludes the effects of WDM signals other than the target signal, cross-phase modulation (XPM) and four-wave mixing (FWM) from signals other than the target signal were not considered. At the transmitter part, the parallelized bit string is converted from bit to symbol using the symbol map after the serial-to-parallel conversion of the original data. Each SC signal is encoded into an FC, PC, or FPCC by the frequency and/or polarization domain in the encoder. The pilot symbol is inserted after coding. Therefore, the 4QAM pilot symbol is uncoded. The average signal power is adjusted after coding. To avoid crosstalk caused by adjacent SC signals, each SC was spectrum-formatted to Nyquist by a digital filter, frequency-shifted, and multiplexed. The SC-multiplexed signal is converted from a digital signal to an analog signal using a digital-to-analog converter. A polarization-multiplexed IQM modulates

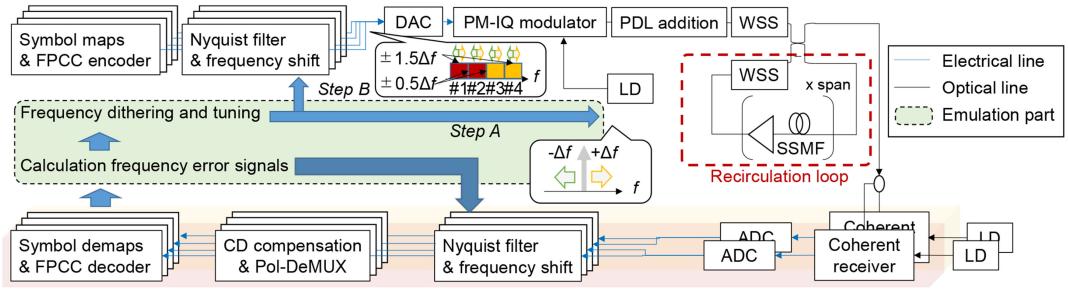

Fig. 7. Simulation setup.

the DP-*M*-QAM signal for a 1550 nm continuous-wave output from a tunable LD connected by a polarization-maintained fiber. After propagating the transmission line through the ROADM network and division by the optical coupler, the received signal was mixed with the local oscillator laser and coherently detected. After the analog-to-digital converter converts the signal from analog to digital, the SC is demultiplexed using the same Nyquist filtering and frequency shift as those on the transmitter side. After performing CD compensation to compensate for the wavelength dispersion of the transmission line, depolarization demultiplexing was performed. Furthermore, the accumulated CD was corrected using a fixed equalizer in the time domain with a finite impulse response (FIR) filter. The tap factor of the FIR filter in the static equalizer sets the pretrained value by extracting the preamble. The adaptive equalizer uses a 4QAM pilot to track the polarization state of the transmitted signal. Then, the compensated symbol is regenerated after separating the data using the FC, PC, or FPCC decoder, and the original bit string is restored from the original QAM symbol. Finally, the average bit error rate (BER) is calculated by counting the bit errors of a single carrier or all 4SC and dividing the value by all transmitted bits. Additionally, the BER was converted to a Q-factor for performance comparison. This simulation assumes that there are no frequency or carrier phase offsets for the proof of concept. Frequency offsets can be estimated by a predetermined angular difference estimation [42] or fast Fourier transform [43]. The carrier phase offset can be removed by blind Viterbi–Viterbi carrier phase retrieval (CPR) and the maximum likelihood algorithm for the Gaussian probabilistic distributed *M*-QAM signal [44]. The error correction code assumes a soft-decision 25.5% overhead forward error correction (FEC) with a threshold of pre-FEC Q is 4.95 dB [45].

We performed a comparative evaluation of four DC-paired multicarrier signals and two single-carrier signals to verify the PDL and PBN tolerances of the proposed FPCC under fiber-nonlinearity conditions. The tested signal types were standard single carriers, single carriers with PC, standard 4SC, 4SC with FC, 4SC with PC, and 4SC with FPCC. The total bit rates for DP-4QAM and DP-16QAM were 224 and 448 Gb/s, respectively. The baud rates of the total and each SC were set to 56 and 14 GBd, respectively. The data patterns were 50000-bit binary sequences. Each SC signal with DP-*M*-QAM was RRC-filtered with a roll-off factor of 0.01.

In this study, DP-4QAM exhibited a high PBN tolerance and high fiber nonlinear tolerance, and hence, all tested signals were inserted into several span transmissions with short reach per span considering 80 spans of 50 km of standard single-mode fiber (SSMF). The PDL is a lump type provided collectively before the fiber transmission. DP-16QAM exhibited a low PBN and fiber nonlinear tolerances, and hence, all tested signals were inserted into a few span transmissions with long reach per span considering 15 spans of 80 km of SSMF. The SSMF exhibited a cumulative loss of 0.25 dB/km or 0.2 dB/km, a CD of 17 ps/nm/km, and a nonlinear index of 1.3 W^{-1} km^{-1}. Polarization mode dispersion was not considered in this study. Erbium-doped fiber amplifiers with a noise figure of 5 dB were used for loss compensation. To emulate the cascaded ROADMs, the transmission characteristics of WSSs in the ROADM node were assumed to be those of a 5th super-Gaussian-shaped optical bandpass filter with a 3 dB bandwidth of 75 or 62.5 GHz, which corresponded to 6 and 5 grids, respectively, when 12.5 GHz is one grid. Fig. 8(a) shows the transmit bandwidth relative to the number of WSSs. As the number of WSSs increased, the transmission bandwidth became narrower. Furthermore, the transmission bandwidth decreased significantly, particularly in areas with low WSS numbers. Fig. 8(b) shows the transmission characteristics of one WSS and 80 cascaded WSSs. As the number of WSSs passed increased, the edges of the transmission spectrum became steeper. Therefore, the signal performance degradation was slightly more significant than that of the original 5th super Gaussian filter under the same bandwidth conditions. Furthermore, it is assumed that there are four SCs and two edge nodes with and without multicarrier frequency control. Here, we consider that: (1) there is no penalty owing to the linear transmission distortion compensation in the access network, (2) there is almost no individual difference between transceivers, and (3) there is no penalty for coherent reception for the reception power. Fig. 9 shows the back-to-back performance comparison of standard DP-4QAM and DP-4QAM signals with 1-D coding such as PC or FC. The probabilistic signal distribution by this coding is different from the probabilistic shaping using the distribution matcher based on the Maxwell-Boltzmann distribution that maximizes the information amount for the SNR [46], and the information amount does not change according to the distribution of the signal points. The SNR after coding is the same as the SNR without coding in the linear region, so the noise tolerance and back-to-back performance of all the cases were almost the same. Therefore, we can confirm that the 1D-coded DP-QPSK signal exhibits the same characteristics as that of the theoretical and simulation

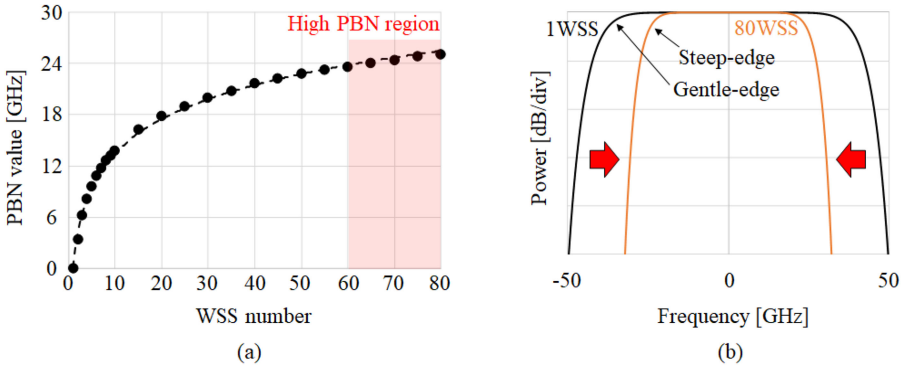

Fig. 8. (a) PBN value for cascaded WSS number. (b) Transmission characteristics after 1 WSS and 80 WSSs.

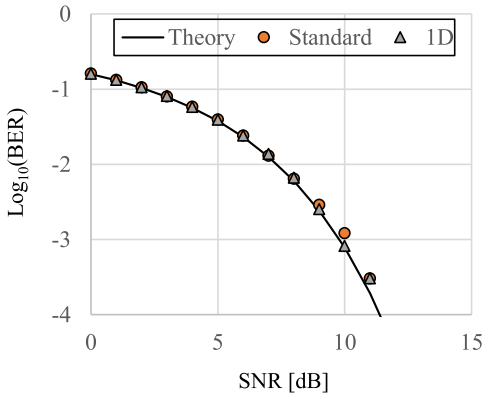

Fig. 9 Back-to-back characteristics of QAM signals with/without multicarrier coding.

values of the normal quadrature phase-shift keying (QPSK) by performing decision processing by maximum likelihood detection.

The proposed multicarrier frequency control method was evaluated using an emulation program that monitored Q noise with a standard deviation of 0.1. The two steps were repeated 1000 times as a single LD drifted rapidly and monotonously by approximately 2.5 GHz in 2.5 h. The number of Q monitoring operations in each control step was set to 10, whereas the dither frequency and time required for each monitoring operation were 1 Hz and 0.5 s, respectively. All WSS assumes that the central frequency of the transmission band does not drift. Since the dither frequency of 1 Hz is low, the delay difference between the dither control signals and the delay difference due to the fiber length difference does not affect the signal characteristics. The effects of frequency fluctuations due to external environmental factors and time fluctuations in the noise around electrical components and optical noise can be considered Q fluctuations during monitoring. We assume that the frequency offset compensation and CPR in the receiver-side DSP can be sufficiently followed [47].

The LD and DSP dither amplitudes Δf were set to 200 MHz and 100 MHz, respectively. Based on the simulation results using frequency detuning, the static and dynamic Q of the DC-paired DP-16QAM signal and all SC frequencies were calculated throughout Steps A and B. Here, a dynamic Q evaluation is performed using 5σ, which is an index of the stability of the Q value over time. The Q value follows a normal distribution, and σ corresponds to the standard deviation. 5σ corresponds to the interval of 99.99994% of the total Q factor.

VI. Static Performance Comparison of Coded Signal Transmission

A. DC-Paired DP-4QAM

Fig. 10(a) shows the Q factor of the transmission distance for a 6 dB PDL. For total fiber transmission distances of 3000, 3500, and 4000 km, the WSS transmissions with a 3 dB bandwidth were 51.6, 50.6, and 50 GHz, respectively. The 4SC with FPCC method, which reduces the probability that the four corners of the signal point will occur during optical fiber transmission, can reduce the optical fiber nonlinear effect and obtain the maximum characteristics. Next, the single carrier with PC method, which has high resistance to band narrowing and PDL, has the second-best attributes at the time of 4000 km transmission. The standard 4SC, which has low-bandwidth narrowing resistance and polarization-dependent loss resistance, has lower Q characteristics than the two single-carrier methods and the other three multi-carrier methods when transmitting 4000 km.

Fig. 10(b) and (c) show each coding scheme and Q factor for each SC as a fiber starting power function over 4000 km with a 6 dB PDL. The Q characteristics of each method at -6 dBm, which is close to the linear region, tend to be close. However, in either case, the linear effects of the PDL and PBN of the fiber involved in the transmission incur a penalty when the input power is -6 dBm. Under the condition of standard 4SC-DP-4QAM signal, the characteristics of MX-SC unaffected by PDL and PBN are consistent with the linear limit of fiber launched power from -6 to -4 dBm. Therefore, it is no deterioration due to the non-linear effect. The Q characteristics of each technique at 0 dBm, where the influence of the nonlinear effect is weak, have the same tendency as in Fig. 10(a). The Q characteristics of each method at 2 dBm, which is strongly affected by fiber nonlinear effects, tend to deteriorate. We can confirm that the four-point signal point arrangement in the standard 4SC has higher fiber nonlinear tolerance than the probabilistic signal point arrangement by coding. In the same coding method, the

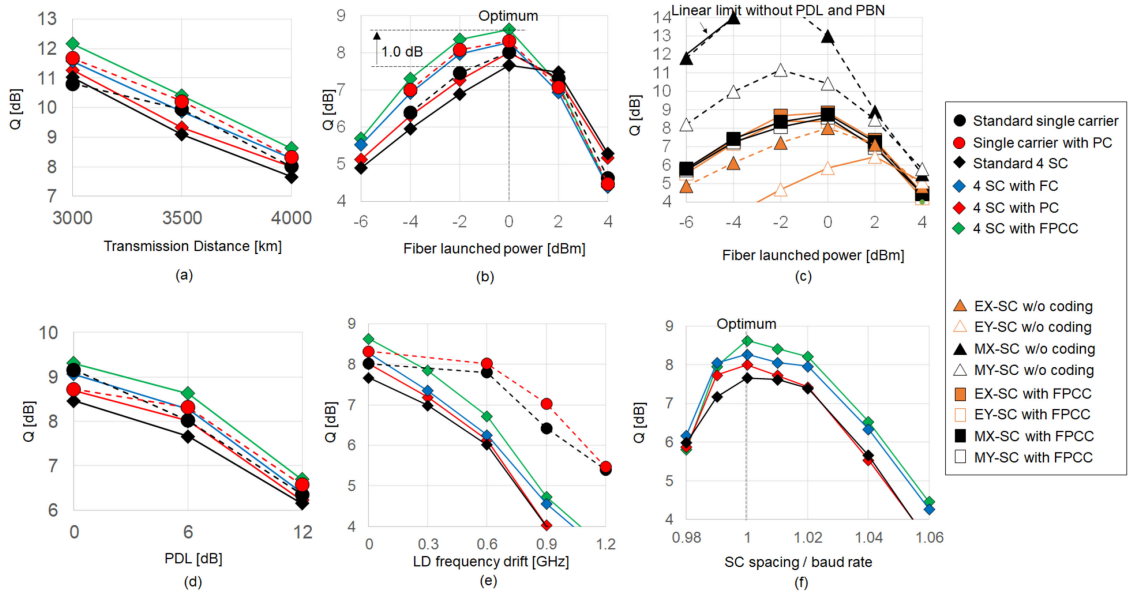

Fig. 10. Static Q factors of DP-4QAM. (a) Transmission performance. (b) Nonlinear tolerance of each coding scheme. (c) Nonlinear tolerance of each SC. (d) PDL tolerance. (e) LD frequency drift tolerance. (f) Filtering and inner-SC interference tolerance.

single-carrier method was superior to the 4SC case considering the PBN decreased the performance of the edge SC, thereby resulting in lower overall characteristics.

For 4SC, the FCPC scheme performed better than the other schemes considering coding was implemented across the frequency or polarization domain. Furthermore, the FPCC method equalizes the self-phase modulation (SPM), XPM, and FWM between the 4SCs at the optimum fiber incident power. Moreover, the FPCC scheme provided a 1 dB improvement from 7.6 dB to 8.6 dB by balancing the optimal fiber launched power of all SCs, as shown in Fig. 10(c).

Fig. 10(d), (e), and (f) show the Q values for PDL, LD frequency drift, internal SC interference, and PBN tolerance assessment over 4000 km transmission. Regardless of the PDL value, the FPCC scheme was superior to the other single-carrier and 4SC methods considering the coding was implemented across the frequency or polarization domain. This coding can equal the optimal fiber-launched power by balancing the effects of SPM, XPM, and FWM. However, the performance of the FPCC scheme decreased significantly owing to the LD frequency drift. In contrast, the single-carrier Q factor was almost stable up to a frequency drift of 0.6 GHz. When the SC spacing was narrow, the Q value of all 4SC signals tested was reduced by internal SC interference. The optimal SC interval was the same as that of the baud rate.

B. DC-Paired DP-16QAM

Fig. 11(a) shows the static Q value at varying node ratios to the WSS at 6 dB PDL. For 2, 3, and 5 nodes per WSS, the WSS passbands with bandwidths of 3 dB were 51.4, 53.2, and 56 GHz, respectively. Although the transmission distance under the condition of 6 dB PDL is the same as that of 1200 km transmission, the optimum coding method must be different considering the effect of bandwidth narrowing is different. A significant effect of bandpass narrowing realizes improved characteristics with a single carrier. In other words, when there is almost no effect of band stenosis, better characteristics are accepted with standard 4SC.

Figs. 11(b) and (c) show the Q factors of each coding and SC as a function of the fiber-launched power under a 6 dB PDL, 3 span/WSS, and 1200 km transmission. Each method at −4 dBm, close to the linear region, has a relative Q characteristic. The Q characteristics of each technique at 0 dBm deteriorate from the linear area and become the characteristics. The Q characteristics of each method under fiber launched power conditions, which are subject to more substantial nonlinear effects, tend to be further degraded. In the case of single-carrier and 4SC, the 16-point signal point arrangement of normal 16QAM tends to have a higher nonlinear tolerance than the stochastic signal point arrangement by coding, so the tendency is the same as that of 4QAM. In the same coding scheme, the single-carrier transmission performed better than the 4SC transmission considering the performance of edge SCs decreased owing to the PBN. In the 4SC transmission, the performances of the frequency-and/or polarization domain coding were better compared to the standard case. Similar to DP-4QAM, the coding was implemented across the frequency or polarization domain, which could equal the optimum fiber-launched power by balancing the SPM, XPM, and FWM effects. The proposed FPCC improved by 0.2 dB from 9.9 to 10.1 dB by balancing the optimum fiber-launched power of all SCs, as shown in Fig. 11(c).

Fig. 11(d), (e), and (f) show the Q factors for the PDL, LD frequency drift, inter-SC interference, and PBN tolerance evaluations under a 1200 km transmission. Regardless of the value of the PDL, 4SC-DP-16QAM with FPCC outperformed the other single-carrier and 4SC schemes. However, its performance was significantly degraded by LD frequency drift. Meanwhile, the Q factor of the single carrier was almost stable until a 1.5 GHz frequency drift. In the narrow SC spacing case, the Q-factors of

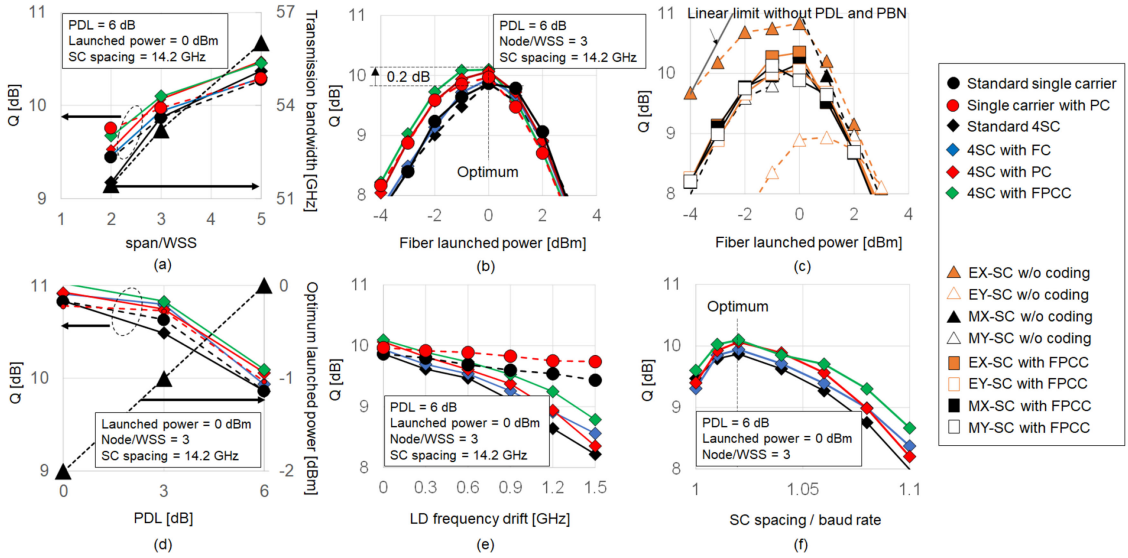

Fig. 11. Static Q factors of DP-16QAM. (a) Span/WSS performance. (b) Launched power tolerance of each coding. (c) Launched power tolerance of each SC. (d) PDL tolerance. (e) LD frequency drift tolerance. (f) Filtering and inter-SC interference tolerance.

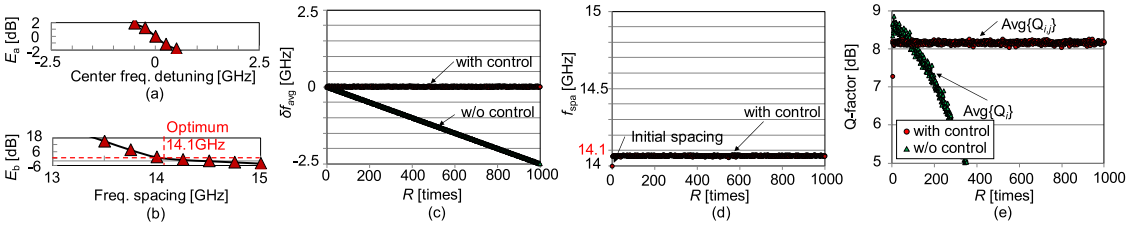

Fig. 12. Dynamic characteristics of DC-paired DP-4QAM with FPCC and multicarrier frequency control. (a) Error signal in Step A. (b) Error signal in Step B. (c) Average frequency detuning. (d) Frequency spacing. (e) Q factor as a function of repetition time R.

all tested 4SC signals were degraded by inter-SC interference. The optimum SC spacing was found to be 14.2 GHz to avoid the effects of inter-SC interference, which was slightly larger than each SC bandwidth.

VII. Dynamic Characteristics With Multicarrier Frequency Control Algorithm

A. DC-Paired DP-4QAM

Fig. 12 shows the dynamic characteristics of 4SC-DP-4QAM using FPCC and multicarrier frequency control when emulating the monotonous drift of the transceiver source frequency. The condition is a 0 dBm launched power, 6 dB PDL, 1 span/WSS, and 4000-km transmission.

Fig. 12(a) and (b) show the error signals for frequency control steps A and B, respectively. Under optimal frequency conditions, the error signal E_s was close to zero, and the polarity of the error signal was inverted at each control step S. As shown in Fig. 12(c) to (e), the average frequency detuning δf_{avg} and frequency interval f_{spa} were almost optimal conditions, respectively, indicating that the results of offline emulation of dynamic LD frequency drift and its self-tuning, except for the initial convergence period when the control repetition time R was less than 100. Therefore, we can confirm that even if the frequency arrangement is initially set from the optimum frequency spacing without frequency control, it converges to the optimum frequency arrangement at the time of frequency control. Considering this, because the characteristic deterioration is large when the frequency interval is narrow, the frequency interval converges wider than the initial frequency spacing.

As shown in Fig. 12(e), Avg$\{Q_{ij}\}$ decreased from 8.6 to 8.2 dB owing to the inter-SC interference in Step B. When no frequency control was applied, Avg$\{Q_i\}$ degraded significantly, and hence, the proposed method yielded a significant improvement. Herein, we define the Q factor as Avg$\{Q_i\}$ for the conventional free-running case and Avg$\{Q_{ij}\}$ for the dithering case. We can confirm stable control is achieved while converging the Q factor fluctuation 5σ at 0.2.

Fig. 13(a)–(c) show the signal characteristic fluctuation of 5σ, average Q factors, and optimum frequency spacing for dither amplitude. As Δf increases, 5σ and Q-factor are affected by inter-SC interference and PBN to the same extent and deteriorates rapidly. In addition, since the transmission conditions are such that the effects of inter-SC interference and PBN are balanced, the optimum average frequency is almost constant at 14 GHz regardless of the dither amplitude.

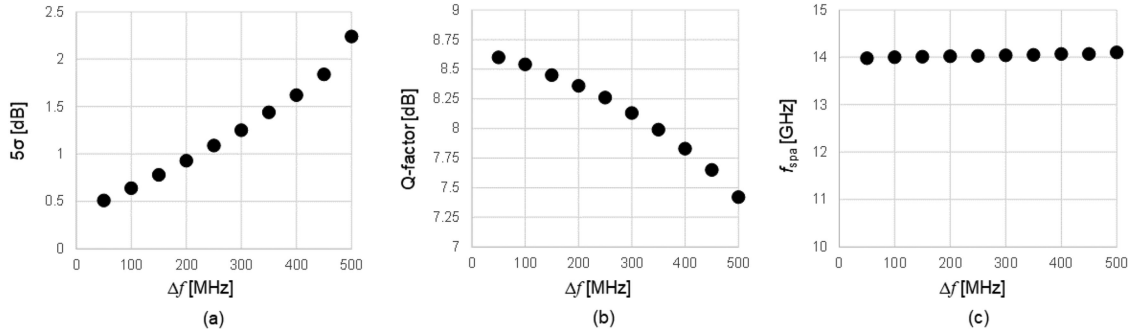

Fig. 13 Dither amplitude load analysis of DC-paired DP-4QAM with FPCC and multicarrier frequency control. (a) 5σ, (b) Q factor, (c) frequency spacing.

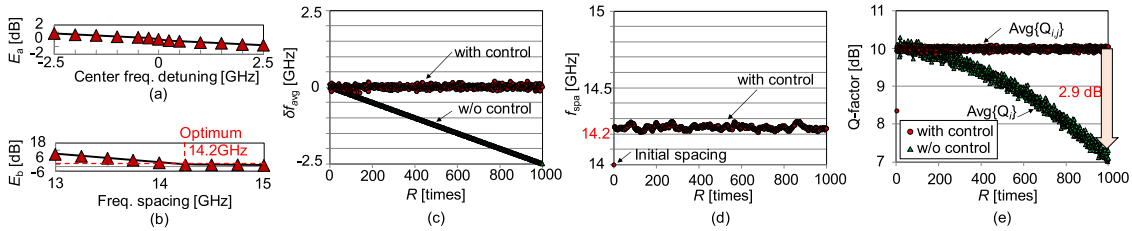

Fig. 14. Dynamic characteristics of DC-paired DP-16QAM with FPCC and multicarrier frequency control. (a) Error signal in Step A. (b) Error signal in Step B. (c) Average frequency detuning. (d) Frequency spacing. (e) Q factors as a function of repetition time *R*.

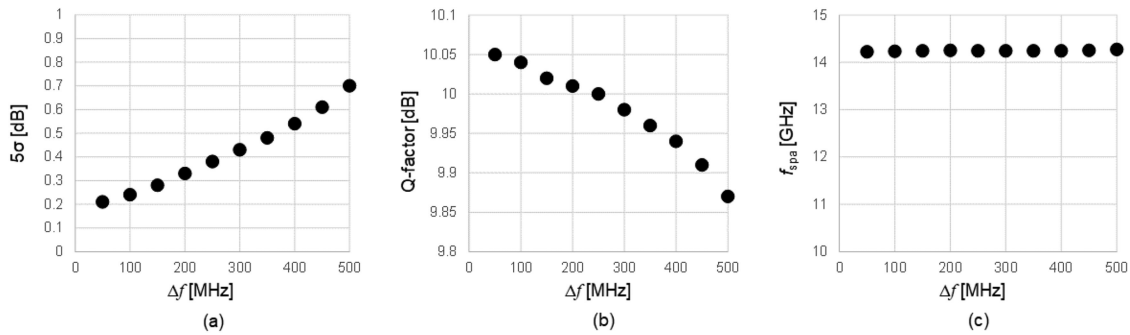

Fig. 15 Dither amplitude load analysis of DC-paired DP-16QAM with FPCC and multicarrier frequency control. (a) 5σ, (b) Q factor, (c) frequency spacing.

B. DC-Paired DP-16QAM

Fig. 14 shows the dynamic characteristics of 4SC-DP-16QAM using FPCC and multicarrier frequency control when emulating the monotonous drift of the transceiver source frequency. The condition was under a 0 dBm launched power, 6 dB PDL, 3 span/WSS, and 1200-km transmission.

Fig. 14(a) and (b) show the error signals in the frequency control steps in steps A and B, respectively. At the optimum frequency arrangement, the error signal E_s was nearly zero, and the polarity of the error signal inverted at each control Step S. Fig. 14(c)–(e) show the offline emulation results for dynamic LD frequency drifts and its self-tuning. Except for the initial convergence period, the average frequency detuning δf_{avg} and frequency spacing f_{spa} were approximately the optimum condition, as shown in Fig. 14(c) and (d), respectively. As mentioned in the previous section, even if the frequency arrangement started from the optimum frequency arrangement without frequency control, we can confirm that the frequency converged to the optimum frequency arrangement during frequency control. Considering this, if the frequency interval is narrow, the characteristic deterioration will be significant, such that the frequency interval will converge at a wider spacing compared to the initial value.

$Avg\{Q_{ij}\}$ decreased from 10.1 dB to 10 dB on average owing to the inter-SC interference in Step B, as shown in Fig. 14(e). When no frequency control was applied, $Avg\{Q_i\}$ decreased to 7.1 dB on average. Therefore, the proposed method yielded a significant improvement of 2.9 dB. We can confirm stable control is achieved while converging the Q value fluctuation 5σ at 0.33. When comparing the results of Q value fluctuations of the 4SC-DP-4QAM signal and the 4SC-DP-16QAM signal, the 4SC-DP-16QAM signal has a slight Q value deterioration for the amount of change in the center optical frequency and the optical frequency interval. Therefore, the accuracy of control based on the error signal becomes low, and the Q value at the time of control becomes large. If the time required for long-term frequency drift is sufficiently longer than the time needed for single monitoring, the Q factor degradation caused by light source drift will be minimal. Therefore, it can be said that the Q value fluctuations that accompany control

are mainly due to the Q value fluctuations that occur during monitoring.

Fig. 15(a)–(c) show the load characteristics for dither amplitude. Compared with the case of DP-4QAM, the transmission distance is short, and the influence of inter-SC interference and PBN is small, so we can confirm that the amount of deterioration of 5σ and Q value for the dither amplitude is also tiny. In addition, since the effect of PBN is small, the optimum frequency also converges at around 14.2 GHz. The optimum subcarrier spacing is larger than the symbol rate of the subcarriers.

VIII. Conclusion

This study proposed two approaches using DSP to reduce PDLs and PBN, which degrade the signal quality in ROADM systems with point-to-multipoint topologies. The feasibility of frequency/polarization concatenated coding and multicarrier frequency control algorithm for cascaded ROADM-filtering-tolerant 200 Gb/s and 400 Gb/s DC-paired DP-M ($M = 4$ and 16)-QAM transmissions were numerically demonstrated. Compared to traditional coding methods and other numbers of SCs, the FPCC scheme for 4SC demonstrated performance improvement when the PBN was neither large nor small under conditions where PDL and fiber nonlinearity occur. In the emulation model assuming long-term LD frequency drifts, the multicarrier frequency control algorithm for cascaded ROADM system with point-to-multipoint topology showed that a Q degradation of less than 0.4 dB could be maintained. When the dither amplitude was small, the frequency spacing during frequency control matched the optimal frequency spacing in the static evaluation. Furthermore, we clarified that even if the optimum frequency interval with and without frequency control differed depending on the emulator, it converged to the optimum frequency spacing with the control immediately after frequency control began. The proposed multicarrier frequency control showed that the 4SC-DP-4QAM signal and the 4SC-DP-16QAM signal operate while keeping the Q value fluctuation 5σ caused by the management at 0.2 and 0.33.

As described above, this study summarizes the influence of one channel consisting of a single carrier and multi-carrier, which is targeted end-to-end, on the relay ROADM node. In the future, we will consider the effects of multiple channels adding and dropping on the cascaded ROADM node for the application to existing systems. Hence, we plan to expand the evaluation under the conditions of the WDM optical transmission system. In summary, the proposed multi-carrier application can be expected to ensure long-term stable operation of various IoT traffic in optical access and metro convergence networks that connect the edge nodes of the access network to the hub boxes of the metro network.

References

[1] J. Back *et al.*, "CAPEX savings enabled by point-to-multipoint coherent pluggable optics using digital subcarrier multiplexing in metro aggregation networks," in *Proc. Eur. Conf. Opt. Commun.*, Brussels, Belgium, Dec. 2020, pp. 1–4.

[2] "XR optics innovative point-to-multipoint coherent that slashes aggregation network TCO," Infinera, San Jose, CA, USA, 2020. [online]. Available: https://www.infinera.com/innovation/xr-optics/

[3] H. Sugaya *et al.*, "CDCG-ROADMs for flexible optical trunk line networks," *Fujitsu Sci. Tech. J.*, vol. 52, no. 2, pp. 83–89, Apr. 2016.

[4] O. Gerstel, M. Jinno, A. Lord, and S.J.B. Yoo, "Elastic optical networking: A new dawn for the optical layer?," *IEEE Commun. Mag.*, vol. 50, no. 2, pp. S12–S20, Feb. 2012.

[5] J. Yu *et al.*, "Transmission of 8 x 480-Gb/s super-Nyquist-filtering 9-QAM-like signal at 100 GHz-grid over 5000-km SMF-28 and twenty-five 100 GHz-grid ROADMs," *Opt. Exp.*, vol. 21, no. 13, pp. 15686–15691, Jan. 2013.

[6] X. Liu, S. Chandrasekhar, B. Zhu, P. J. Winzer, A. H. Gnauck, and D. W. Peckham, "448-Gb/s reduced-guard-interval CO-OFDM transmission over 2000 km of ultra-large-area fiber and five 80-GHz-Grid ROADMs," *IEEE J. Lightw. Tecnnol.*, vol. 29, no. 4, pp. 483–490, Feb. 2011.

[7] T. Kodama and M. Hanawa, "Dual-phase-conjugation coded digital multi-carrier transmission for long-haul coherent optical systems," in *Proc. Conf. Lasers Electro. Opt.*, San Jose, CA, USA, May 2018, pp. 1–2.

[8] V. A. J. M. Sleffer *et al.*, "Transmission of 448-Gb/s dual-carrier POLMUX-16QAM over 1230 km with 5 flexi-grid ROADM passes," in *Proc. Opt. Fiber Commun. Conf. Exhib.*, Los Angeles, CA, USA, Mar. 2012, pp. 1–3.

[9] F. Buchali, W. Idler, N. Rastegardoost, T. Drenski, R. Ward, and L. Zhao, "Preemphased prime frequency multicarrier bases ENOB assessment and its application for optimizing a dual-carrier 1-Tb/s QAM transmitter," in *Proc. Opt. Fiber Commun. Conf. Exhib.*, Anaheim, CA, USA, Mar. 2016, pp. 1–3.

[10] L. B. Du and A. J. Lowery, "Improved single channel backpropagation for intra-channel fiber nonlinearity compensation in long-haul optical communication systems," *Opt. Exp.*, vol. 18, no. 16, pp. 17075–17088, Aug. 2010.

[11] E. Giacoumidis *et al.*, "Comparison of DSP-based nonlinear equalizers for intra-channel nonlinearity compensation in coherent optical OFDM," *Opt. Lett.*, vol. 41, no. 11, pp. 2509–2512, May 2016.

[12] W. Shieh and Y. Tang, "Ultrahigh-speed signal transmission over nonlinear and dispersive fiber optic channel: The multicarrier advantage," *IEEE Photon. J.*, vol. 2, no. 3, pp. 276–283, Jun. 2010.

[13] H. Nakashima, T. Tanimura, T. Oyama, Y. Akiyama, T. Hoshida, and J. C. Rasmussen, "Experimental investigation on nonlinear tolerance of subcarrier multiplexed signals with spectrum optimization," in *Proc. Eur. Conf. Opt. Commun.*, Valencia, Spain, Sep. 2015, pp. 1–3.

[14] G. Bosco, V. Curri, A. Carena, P. Poggiolini, and F. Forghieri, "On the performance of Nyquist-WDM terabit superchannels based on PM-BPSK, PM-QPSK, PM-8QAM or PM-16QAM subcarriers," *IEEE J. Lightw. Technol.*, vol. 29, no. 1, pp. 53–61, Jan. 2011.

[15] D. Welch *et al.*, "Point-to-multipoint optical networks using coherent digital subcarriers," *IEEE J. Lightw. Technol.*, vol. 39, no. 16, pp. 5232–5247, Aug. 2021.

[16] D. Lavery *et al.*, "Opportunities for optical access network transceivers beyond OOK," *IEEE J. Lightw. Technol.*, vol. 11, no. 2, pp. A186–A195, Feb. 2019.

[17] J. Zhang, Z. Jia, H. Zhang, M. Xu, J. Zhu, and L. Alberto, "Rate-flexible single-wavelength TFDM 100G coherent PON based on digital subcarrier multiplexing technology," in *Proc. Opt. Fiber Commun. Conf. Exhib.*, San Diego, CA, USA, Mar. 2020, pp. 1–3.

[18] T. Kodama, K. Shimada, R. Matsumoto, T. Inoue, S. Namiki, and M. Jinno, "Frequency-packed multiband-coherent transceiver with symbol rate-adaptive Nyquist WDM signals," *IEEE Photon. Technol. Lett.*, vol. 33, no. 21, pp. 1205–1208, Nov. 2021.

[19] O. Vassilieva, S. Oda, T. Hoshida, J. C. Rasmussen, and M. Sekiya, "Experimental investigation of the statistics of the interplay between nonlinear and PDL effects in polarization multiplexed systems," in *Proc. Opt. Fiber Commun. Conf. Expo. Nat. Fiber Optic Engineers Conf.*, Anaheim, CA, USA, Mar. 2013, pp. 1–3.

[20] T. Oyama, H. Nakashima, Y. Nomura, G. Huang, T. Tanimura, and T. Hoshida, "PDL mitigation by polarization-time codes with simple decoding and pilot-aided demodulation," in *Proc. Eur. Conf. Opt. Commun.*, Sep. 2018, pp. 1–3.

[21] J. M. Fabrega *et al.*, "On the filter narrowing issues in elastic optical networks," *IEEE J. Opt. Comm. Netw.*, vol. 8, no. 7, pp. A23–A33, Jul. 2016.

[22] Y.-T. Hsueh *et al.*, "Passband narrowing and crosstalk impairments in ROADM-enabled 100G DWDM networks," *IEEE J. Lightw. Technol.*, vol. 30, no. 24, pp. 3980–3986, Dec. 2012.

[23] D. Ranfique and A. D. Ellis, "Nonlinear and ROADM induced penalties in 28 Gbaud dynamic optical mesh networks employing electronic signal processing," *Opt. Exp.*, vol. 19, no. 18, pp. 16739–16748, Aug. 2011.

[24] T. K. Akino *et al.*, "Han-Kobayashi and dirty-paper coding for superchannel optical communications," *IEEE J. Lightw. Tecnnol.*, vol. 33, no. 7, pp. 1292–1299, Apr. 2015.

[25] C. Zhu, B. Corcoran, L. Zhuang, and A. J. Lowery, "Doubling the ROADM sites using pairwise coding for 4%-guard-band superchannels," in *Proc. Opt. Fiber Commun. Conf. Exhib.*, Anaheim, CA, USA, Mar. 2016, pp. 1–3.

[26] Y. Kawaguchi and T. Tsuritani, "Filtering tolerance of 512-Gb/s dual-carrier PDM-16QAM signals in 75-GHz-Grid ROADM networks," in *Proc. Opto Electron. Commun. Conf.*, Shanghai, China, Jul. 2015, pp. 1–3.

[27] K. Shibahara, A. Matsuda, H. Kishikawa, S. Kawai, and M. Fukutoku, "Filtering-tolerant transmission by the Walsh-Hadamard transform for super-channel beyond 100 Gb/s," *Opt. Exp.*, vol. 23, no. 10, pp. 13245–13254, May 2015.

[28] M. Dallaglio *et al.*, "Demonstration of a SDN-based spectrum monitoring of elastic optical networks," in *Proc. Opt. Fiber Commun. Conf. Exhib.*, Los Angeles, CA, USA, Mar. 2017, pp. 1–2.

[29] G. Nakagawa, S. Oda, K. Sone, Y. Aoki, T. Hoshida, and J. C. Rasmussen, "Demonstration of integrated optical path monitoring sub-system in CDCG-ROADM," in *Proc. Eur. Conf. Opt. Commun.*, Sep. 2014, pp. 1–3.

[30] G. Huang *et al.*, "Precise sub-carrier frequency monitor and control method for superchannel transmission in cascaded ROADM network," in *Proc. Eur. Conf. Opt. Commun.*, Dusseldorf, Germany, Sep. 2016, pp. 1–3.

[31] M. Xiang *et al.*, "Filtering tolerant digital subcarrier multiplexing system with flexible bit and power loading," in *Proc. Opt. Fiber Commun. Conf. Exhib.*, Los Angeles, CA, USA, Mar. 2017, pp. 1–3.

[32] T. Rahman *et al.*, "Digital subcarrier multiplexed hybrid QAM for data-rate flexibility and ROADM filtering tolerance," in *Proc. Opt. Fiber Commun. Conf. Exhib.*, Anaheim, CA, USA, Mar. 2016, pp. 1–3.

[33] A. M. R. Brusin, F. P. Guiomar, A. L-Riesgo, P. P. Monteiro, and A. Carena, "Enhanced resilience towards ROADM-induced optical filtering using subcarrier multiplexing and optimized bit and power loading," *Opt. Exp.*, vol. 27, no. 21, pp. 30710–30725, Oct. 2019.

[34] M. Binkai, T. Kodama, T. Yoshida, Y. Noguchi, N. Suzuki, and K. Motoshima, "Frequency-domain hybrid N x 100 Gb/s regular QAMs for simple, scalable, and transparent software-defined optical transport," in *Proc. Opt. Fiber Commun. Conf. Exhib.*, Los Angeles, CA, USA, Mar. 2017, pp. 1–3.

[35] T. Kodama, M. Binkai, and T. Yoshida, "Simple frequency-domain hybrid-QAM superchannel with path-fitted pre-filtering and collaborative-subcarrier frequency self-tuning for flexible ROADM systems," in *Proc. Opt. Fiber Commun. Conf. Exhib.*, Los Angeles, CA, USA, Mar. 2017, pp. 1–3.

[36] D. Che and W. Shieh, "Entropy-loading: Multi-carrier constellation-shaping for colored-SNR optical channels," in *Proc. Opt. Fiber Commun. Conf. Exhib.*, Los Angeles, CA, USA, Mar. 2017, pp. 1–3.

[37] T. Kodama and M. Hanawa, "Coupled-subcarrier frequency and polarization coded probabilistic constellation for ROADM systems," in *Proc. ACP*, Guangzhou, China, Nov. 2017, pp. 1–3.

[38] T. Kodama, "Robust 400G digital multiband transmission using frequency/polarization concatenated code and frequency-self-tuning algorithm for ROADM system," in *Proc. ACP*, Hangzhou, China, Nov. 2018, pp. 1–3.

[39] T. Mukaihara, T. Kimura, and H. Koshi, "Future narrow linewidth lasers," in *Proc. Opt. Fiber Commun. Conf. Exhib.*, Los Angeles, CA, USA, Mar. 2015, pp. 1–3.

[40] T. Kodama and M. Hanawa, "Robust multiband frequency-tuning algorithm for cascaded ROADM filtering," in *Proc. Conf. Lasers Electro Opt. Pacific Rim*, Hong Kong, Aug. 2018, pp. 1–2.

[41] K. Honda *et al.*, "Wavelength control method of upstream signals using AMCC in WDM-PON for 5G mobile fronthaul," *Opt. Exp.*, vol. 27, no. 19, pp. 26749–26756, Sep. 2019.

[42] L. Li, Z. Tao, S. Oda, T. Hoshida, and J. C. Rasmussen, "Wide-range accurate and simple digital frequency offset compensator for optical coherent receivers," in *Proc. Opt. Fiber Commun. Conf. Exhib.*, San Diego, CA, USA, Mar. 2008, pp. 1–3.

[43] M. Selmi, Y. Jaouen, and P. Ciblat, "Accurate digital frequency offset estimator for coherent PolMux QAM transmission systems," in *Proc. 35th Eur. Conf. Opt. Commun.*, Vienna, Austria, Sep. 2009, pp. 1–2.

[44] X. Li, J. Xiao, and J. Yu, "Heterodyne detection and transmission of 60-Gbaud PDM-QPSK signal with SE of 4b/s/Hz," *Opt. Exp.*, vol. 22, no. 8, pp. 9307–9313, Apr. 2014.

[45] K. Sugihara, S. Kametani, K. Kubo, T. Sugihara, and W. Matsumoto, "A practicable rate-adaptive FEC scheme flexible about capacity and distance in optical transport networks," in *Proc. Opt. Fiber Commun. Conf. Exhib.*, Anaheim, CA, USA, Mar. 2016, pp. 1–3.

[46] J. Cho *et al.*, "Trans-atlantic field trial using high spectral efficiency probabilistically shaped 64-QAM and single-carrier real-time 250-Gb/s 16-QAM," *IEEE J. Lightw. Tecnnol.*, vol. 36, no. 1, pp. 103–113, Jan. 2018.

[47] G. Nakagawa *et al.*, "Demonstration of FSK light label receiver prototype for light path tracing of 112 Gbps DP-QPSK signal," in *Proc. 39th Eur. Conf. Exhib. Opt. Commun.*, London, U.K., Sep. 2013, pp. 1–3.